Geophys. J. Int. (1996) **125,** 15–29

Broad-band modelling of regional seismograms: the Basin and Range crustal structure

Xi J. Song, Donald V. Helmberger and L. Zhao
Seismo Lab, California Institute of Technology, Pasadena, CA 91125, USA

Accepted 1995 October 3. Received 1995 October 2; in original form 1995 May 19

SUMMARY

Three-component broad-band displacement seismograms with paths sampling the Basin and Range province are studied to constrain the crustal structure. To find an average model that fits the data in both absolute time and waveform, we generate broad-band reflectivity synthetics and conduct sensitivity tests on different parts of a layered crustal model, where only a few layers are involved. Generalized rays are used to help identify the various phases. It proves useful to decompose a regional seismogram into segments so that the impact of model parameters on each segment can be clearly identified. Thus, for mid-crustal earthquakes, it is established that the top crustal layer controls the Rayleigh wave, the Airy phase, in shape over the range from 300 to 600 km, and the crustal layer just above the source depth controls its timing. The P_{nl} waves, the P_n and P_L portion, are controlled in broad-band character by the mid-crust while the top layer contributes to their long-period motion. These crustal parameters control the tangential motion similarly. The SV wave, the segment between the P_{nl} wave and the Rayleigh wave, is mostly controlled by the shear velocity of the lower crust. In judging the goodness of fit between the array observations and synthetic waveforms, we allow individual data segments to shift relative to the 1-D synthetics by a few seconds to account for some lateral variation. The amount of time shift is found by the cross-correlation in displacement between the data segment and the synthetics. Applying these tests in a forward modelling approach, we find that a simple two-layer crustal model is effective in explaining this data set. In this model, the main crustal layer has P and S velocities of 6.1 km s^{-1} and 3.6 km s^{-1}, similar to those found by Langston & Helmberger (1974). A surface layer of thickness 2.5 to 3.5 km is required to fit the Rayleigh waves. The refined model can be used as a reference model for further studies in this region.

Key words: Basin and Range, broad band, crustal structure, seismograms.

INTRODUCTION

Recent advances in high-dynamic-range digital instrumentation are allowing dramatic improvements in our ability to estimate seismic characteristics from regional seismograms. This is demonstrated by the introduction of a number of new analytical tools used in estimating source parameters from such data. For example, it is possible to invert regional surface waves at periods greater than 50 s for events with $M_s > 5$ throughout the western United States with one simple model (Ritsema & Lay 1993). For smaller events, the long-period excitation becomes noisy and the body waves become more prominent. Methods that are more sensitive to body waves have been introduced by Dreger & Helmberger (1993) and Zhao & Helmberger (1994). In many cases one station is sufficient to estimate those parameters with a proper crustal model (e.g. Dreger & Helmberger 1993).

The method used by Zhao & Helmberger (1994) involves a direct grid search over the source parameter space (strike, dip, rake), in which observed and synthetic broad-band seismograms are decomposed into segments and the corresponding data and synthetic segments are compared. In their method, the P-wave windows and the S-wave windows are allowed to have a relative time shift between them, which desensitizes the solution to the crustal model used in generating the synthetics. A demonstration of the usefulness of this approach in the estimation of the source mechanism of the 1993 April 29 Arizona event (Zhao & Helmberger 1996) is displayed in Fig. 1. The TERRAscope stations and the event location are shown in Fig. 2, along with other events investigated in this study. The cross-correlation between data and synthetics requires that the synthetic P_{nl} waves be shifted ahead by an average of less than 1 s, the Rayleigh waves by about 5 s and

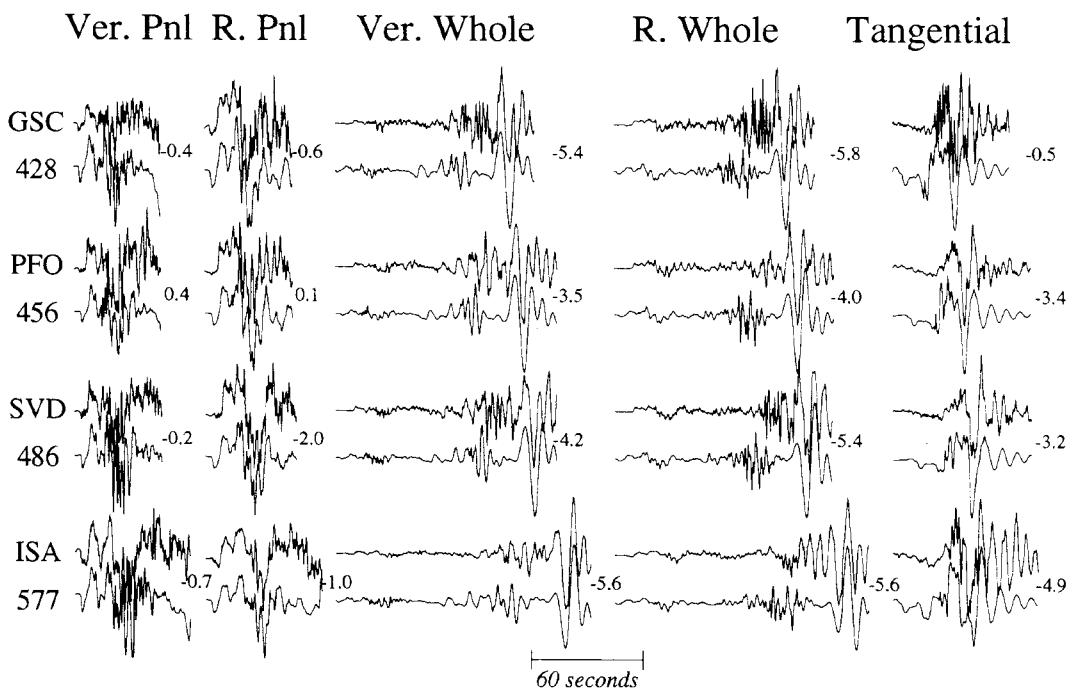

Figure 1. Comparison between the broad-band displacement data (upper traces) and the corresponding best-fitting synthetic waveforms (lower traces) for the Arizona earthquake. Letters on the left-hand side of the figure indicate station names and numbers, the distance from the event. The small numbers indicate, in seconds, the time shift of the synthetic waveforms relative to the data. A positive number indicates that the synthetic is early. After Zhao & Helmberger (1996, reprinted with kind permission of Birkhäuser Verlag, Switzerland).

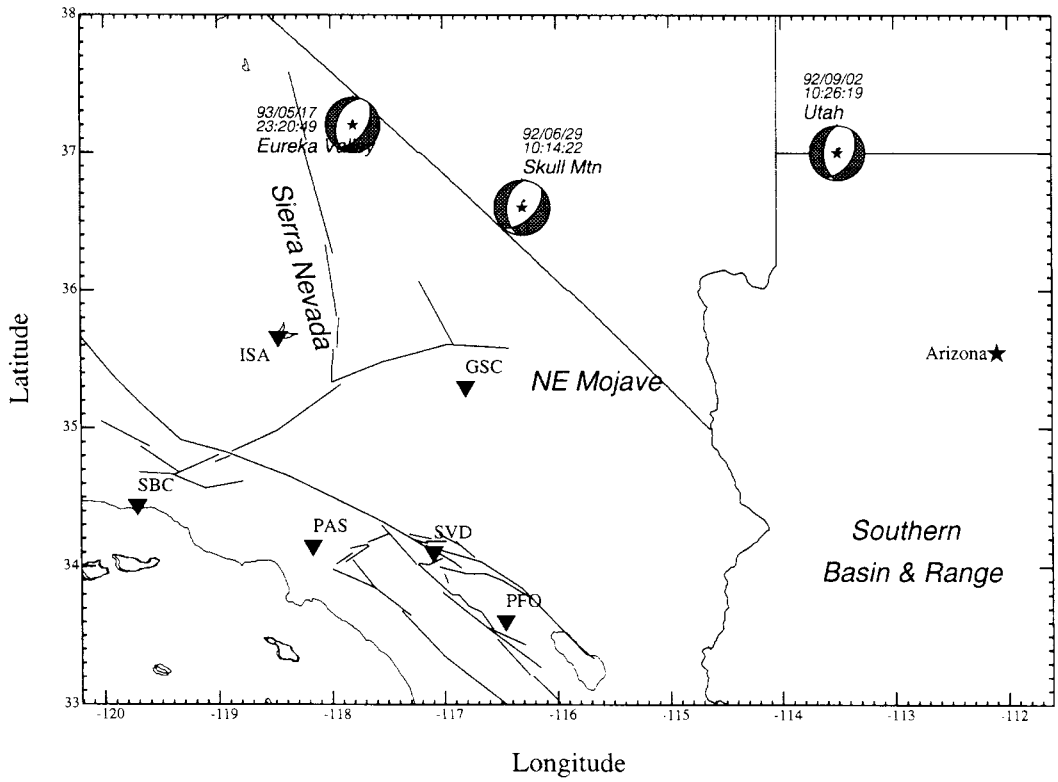

Figure 2. Map of the southwestern United States showing the locations of the events (stars) and some TERRAscope stations (triangles) used in this study. The station Tucson (TUC; 110.78W, 32.31N) is off the map. Origin time and source mechanism for the events used in this study are also shown.

the Love waves by about 3 s. In this sense, the model Zhao & Helmberger (1996) used [Table 1, model *PB* (Priestley & Brune 1978)] is reasonable for the P_{nl} waves but is too slow to match the surface waves along these paths. Also, the separations between the synthetic *P*-wave train and the Rayleigh waves are larger than those observed. However, by applying the segmentation technique, they were able to use these synthetics effectively in their source estimation (Zhao & Helmberger 1996).

While the above technique appears to be effective in source estimation, it could also be useful in establishing creditable crustal models. Present strategies in model determination typically use trial-and-error search procedures or perhaps waveform inversion techniques. These methods compare whole seismograms against synthetics in a least-squares sense and determine the best set of 1-D model parameters. Since the surface waves are the strongest in a seismogram, they dominate the solution. However, the surface waves, especially their timing, are particularly influenced by lateral variation in the shallow crust, as demonstrated by Stead (1990). Perhaps a useful alternative approach would be to search for a 1-D model that fits the segmented wave shapes and minimizes the absolute traveltime shift between data and synthetics for individual segments. We will investigate such an approach in this paper, where we find that simple crustal models prove effective in modelling the Basin and Range crustal structure.

MODEL SENSITIVITIES

The usual situation facing waveform modellers is similar to that in the Arizona example discussed in the last section; that is, to determine the nature of the seismic source with inadequate crustal models. Thus, we would like to learn from the time shifts and the shape mismatch in Fig. 1 how to infer a better model. For example, which model parameter is the most effective in moving the Rayleigh waves or in fixing the *SV* mismatch? To address such issues, we will conduct a set of sensitivity tests on some simple models. For these tests, a double-couple source with strike 180°, dip 50° and rake 250°, which is typical for events studied in this paper, is used. We use a seismic moment of 1.0×10^{20} N m and a far-field source time function described by a triangle (0.5 s, 0.5 s). The source depth is 11 km, and the receiver is located at a distance of 460 km from the source, with a source–receiver azimuth of 226°. The waveform complexities in regional seismograms produced by shallow events can be very difficult to model (e.g. Zhao & Helmberger 1996) and will be avoided in this study.

The making of a regional seismogram

One way to appreciate how a 1-D seismogram is constructed is to use the generalized ray theory (GRT; Helmberger 1983) to compute synthetic waveforms for individual arrivals and observe the interplay between different rays. Another way is to compute complete synthetic seismograms, say with the reflectivity method, starting from models of one layer over a half-space and introducing more complexity by adding deeper discontinuities. In the tests presented here, we use a modified frequency–wavenumber algorithm (Saikia 1994) to compute complete seismograms and use generalized rays to analyse phase information.

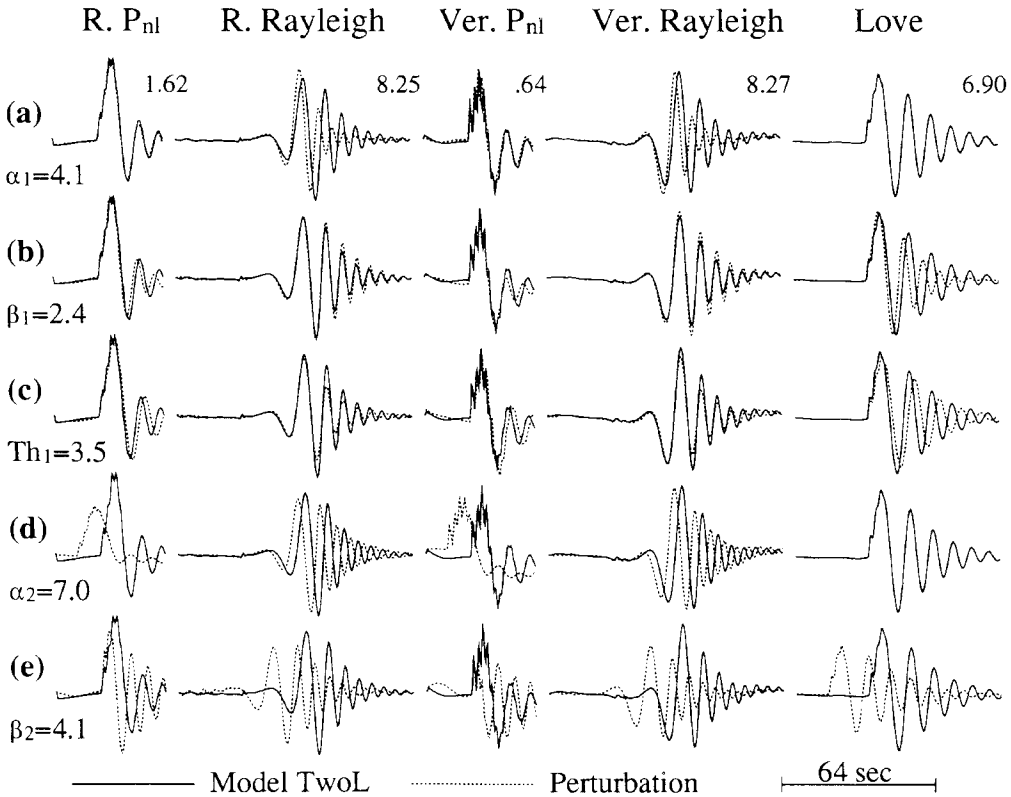

Figure 3. Comparison of synthetic displacement waveforms between model *TwoL* and a series of perturbed models. Only one parameter is perturbed in each test (a–e), with the perturbed parameter shown for the perturbed model. Each section of seismograms is scaled according to the solid trace with peak amplitude shown in centimetres.

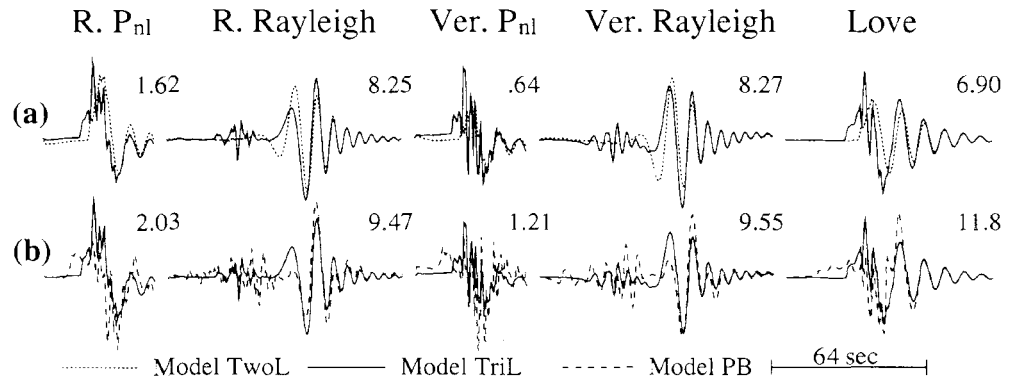

Figure 4. Comparison of synthetic displacement waveforms between models *TwoL*, *TriL* and *PB* (Table 1). Each pair of seismograms is plotted on the same scale. The peak amplitude (cm) of seismograms for model *TwoL* is shown in (a) and that for model *TriL* is shown in (b).

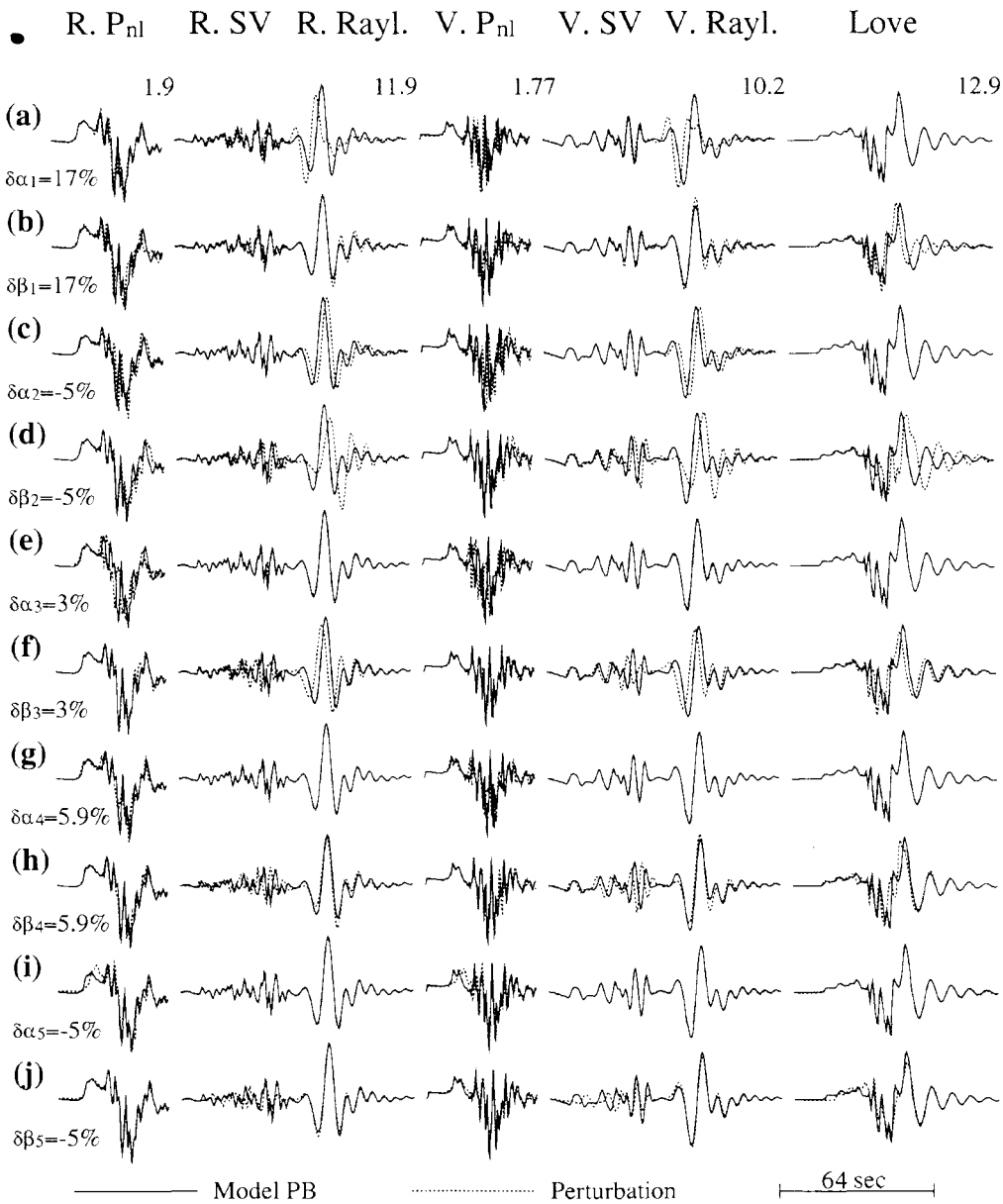

Figure 5. Comparison of synthetic displacement waveforms between model *PB* and a series of perturbed models. Only one parameter is perturbed in each test (a–j), with the perturbed parameter shown for the perturbed model. Each section of seismograms is scaled according to the solid trace with peak amplitude shown in centimetres.

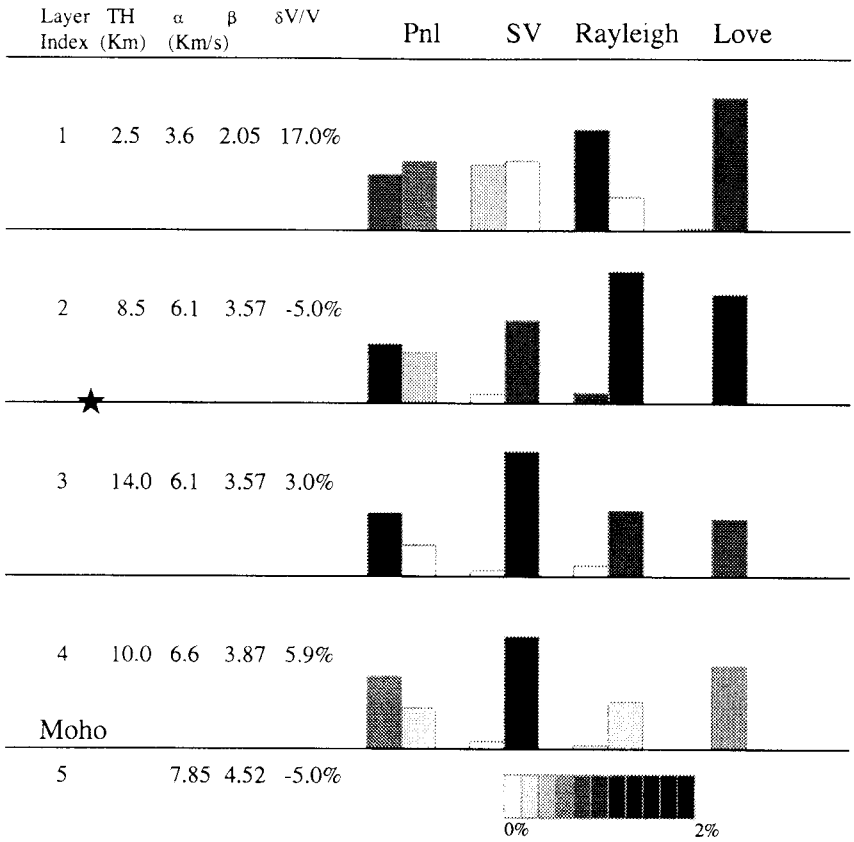

Figure 6. Summary of the effects of different parts of a layered model on a regional seismogram. The parameters of the original model and the amount of velocity perturbation are shown to the left. Each pair of boxes corresponds to the V_p and V_s of that layer. The height of the boxes represents the shape effect (see text) and the shade of the boxes represents the time shift in traveltime percentage. In the Love-wave column, the boxes corresponding to V_p have zero height. The star indicates the source location.

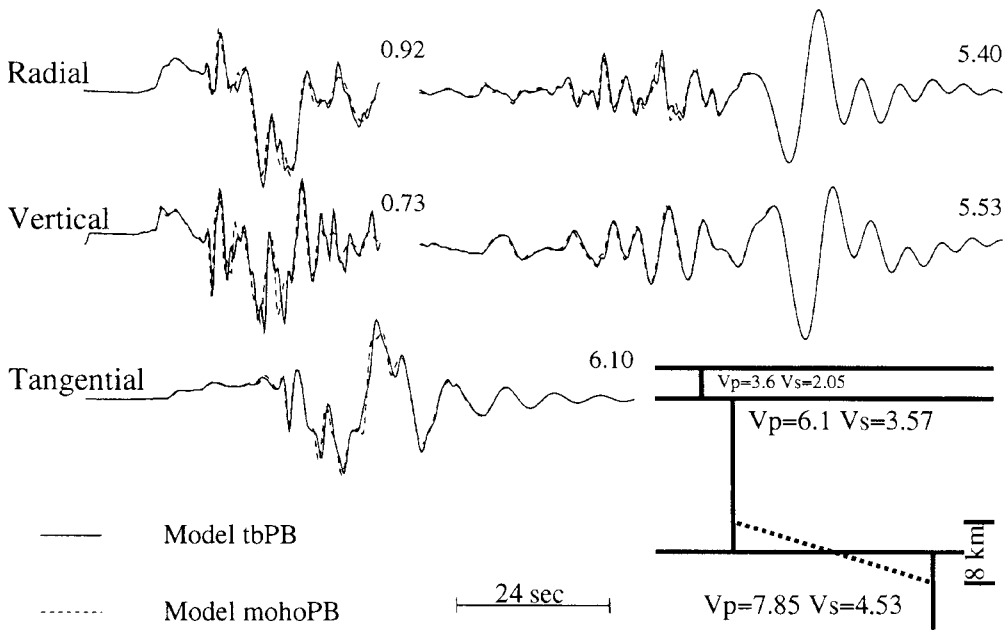

Figure 7. Comparison of synthetic displacement waveforms between models *tbPB* and *mohoPB*. The two models (lower right) differ in the fact that model *tbPB* has a sharp Moho while model *mohoPB* has an 8 km thick transition zone between the crust and the mantle. Each pair of seismograms is plotted on the same scale, with the peak amplitude of the solid trace shown.

Table 1. Model parameters.

Model	V_p km s^{-1}	V_s km s^{-1}	ρ g cm^{-3}	Thickness km
TwoL	3.6	2.05	2.2	2.5
	6.1	3.57	2.8	
TriL	3.6	2.05	2.2	2.5
	6.1	3.57	2.8	22.5
	6.6	3.87	2.9	
PB	3.6	2.05	2.2	2.5
	6.1	3.57	2.8	22.5
	6.6	3.87	2.9	10.0
	7.85	4.53	3.3	
tbPB	3.6	2.05	2.2	2.5
	6.1	3.57	2.8	32.5
	7.85	4.53	3.3	
t58PB	3.6	2.05	2.2	2.5
	5.8	3.57	2.8	32.5
	7.85	4.53	3.3	
tn1PB	3.6	2.05	2.2	2.5
	6.1	3.57	2.8	32.5
	7.85	4.53	3.3	10.0
	7.70	4.53	3.3	10.0
	7.55	4.53	3.3	10.0
	7.4	4.53	3.3	

For two-layer models (Model *TwoL*, Table 1), surface waves are very simple (Fig. 3), but body waves already show some complexity. Our GRT analysis reveals that the first 30 s of the body wave is mainly direct *P*, *P*-to-*S* converted at the interface, and multiples that bounce between the free surface and the layer interface. Among these, rays ending up with a *P* motion are of high frequency and tend to contribute mostly to the vertical component due to the large velocity contrast at the interface. Those ending up with an *SV* motion are usually stronger and have relatively longer duration and contribute more to the radial component. Thus, the vertical component of the broad-band body waves for this simple model at regional distance shows more high-frequency content but weaker motion compared to the radial component.

The *SV* wave, or the segment between the P_{nl} wave and the surface wave on these seismograms, is barely seen and the body-wave energy is dominated by the up-going *P* waves. It is quite clear, in Figs 3(a) and (b), that the change of the compressional wave velocity, V_p, of the top soft layer changes the shape, or the frequency content, of the Rayleigh waves in a very simple fashion, such that the seismograms are compressed with the beginning portion relatively fixed in time. The shear-wave velocity, V_s, of the top layer controls the Love waves in a similar manner. It has a smaller effect on the Rayleigh waves than V_p. On the P_L part that is guided by the top layer, V_s of the top layer has stronger effect than

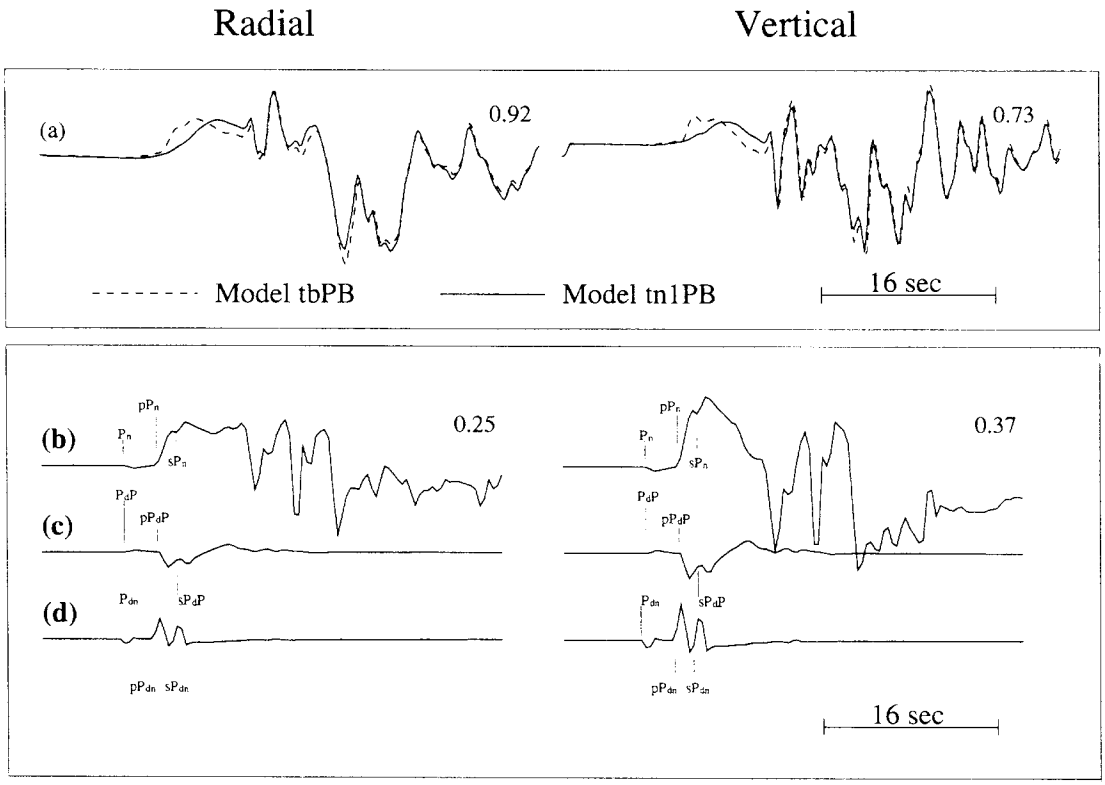

Figure 8. (a)–(c) Effects of a negative velocity gradient in the uppermost mantle. (a) Comparison of the P_{nl} portion of the synthetic displacement waveforms between model *tbPB* and model *tn1PB*. Each pair of seismograms is scaled according to the solid trace with the peak amplitude shown. (b) A set of Moho-reflected rays calculated for model *tbPB* with GRT. (c) A set of rays reflected from a deeper discontinuity 10 km below the Moho, where the *P* velocity drops from 7.85 to 7.7 km s^{-1}. (d) Effects of a positive velocity gradient in the uppermost mantle. Shown here is a set of rays reflected from a deeper discontinuity 10 km below the Moho, where the *P* velocity jumps from 7.85 to 8.0 km s^{-1}. Seismograms in (b)–(d) are scaled according to the ones in (b), with the peak amplitude shown. The subscript d denotes a reflected wave from the deeper discontinuity, and the subscript dn denotes a head wave associated with this discontinuity.

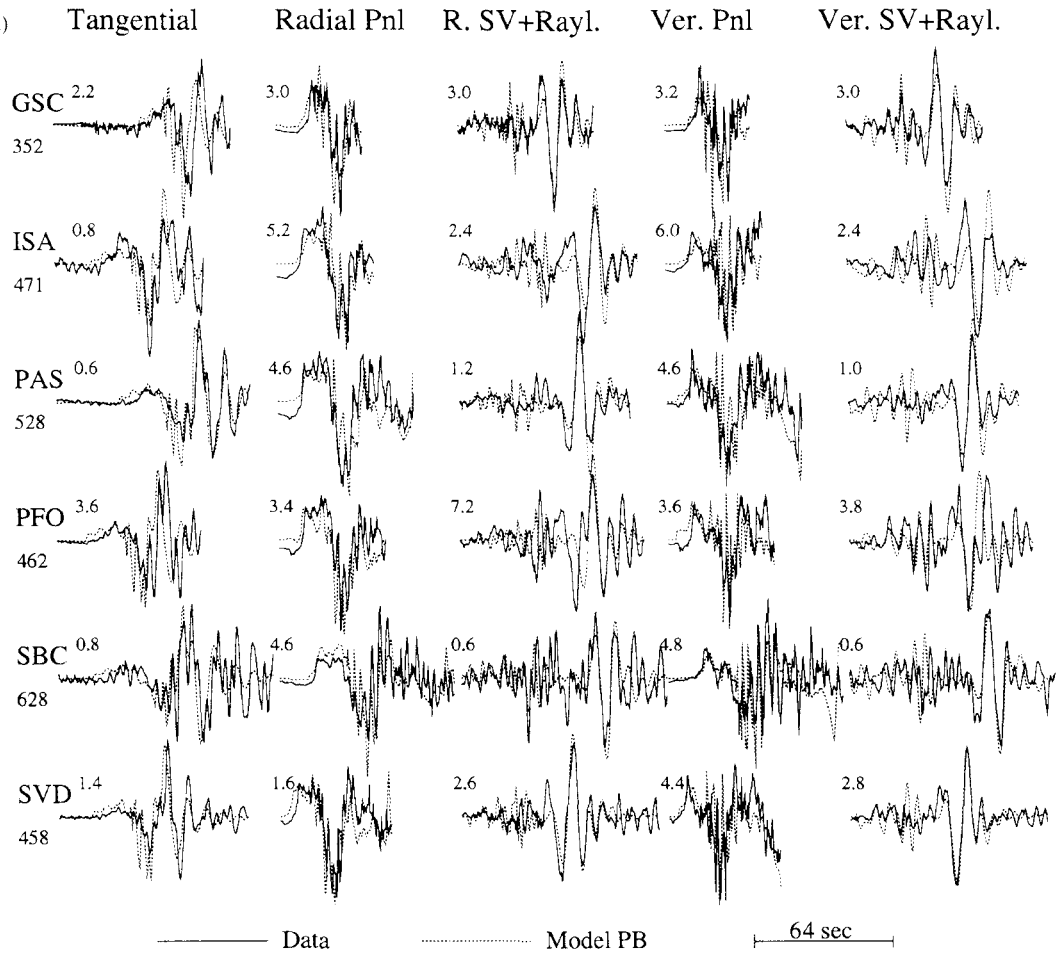

Figure 9. (a) Comparison between displacement data and synthetic waveforms (Model *PB*) for the Utah event. The small number at the beginning of each pair indicates the time shift (in seconds) required for the synthetic waveform to fit the data. Station names and distance from the event are shown on the left-hand side of the diagram. (b) Comparison between displacement data and synthetic waveforms (Model *tbPB*) for the Utah event. (c) Comparison between displacement data and synthetic waveforms (Model *t58PB*) for the Utah event. (d) Shape misfit, represented by the height of the boxes, between data and synthetic waveforms for models *PB*, *tbPB*, and *t58PB* for the Utah event. Station names and distance from the event are also shown.

V_p. The thickness of the top layer affects both the surface-wave part and the body-wave part (Fig. 3c), and the Love waves are more sensitive to this shallow perturbation than the Rayleigh waves, which is what we would expect from the basic construction of these two wave types. The trade-off between the velocity and the layer thickness can be seen by comparing Fig. 3(b) with Fig. 3(c).

In Figs 3(d) and 3(e), the V_p and V_s of the half-space are increased by 14 per cent each. Although these perturbations are no more than those in Figs 3(a) and (b), the seismograms change dramatically. In the surface-wave part, unlike the cases for the top layer, change is more in terms of timing, rather than in wave shape. If the surface waves of the seismograms were allowed to shift a little, they would fit quite well with their counterparts. Change in the P_{nl} wave part is more complicated, both in timing and in shape. However, one can still see that V_p alone controls the earliest part of the body wave and V_s contributes to the later segment, P_L. This shows that the V_p structure can be modelled with the earliest part of data.

The effect of adding a deeper discontinuity to a simple model is shown in Fig. 4. As discussed in detail in Helmberger *et al.* (1993), *SV* waves in this range are dominated by the down-going *SV* energy that is reflected back by the deeper crustal structure. This feature is clearly seen in these seismograms, as the *SV* waves are much stronger than those in Fig. 3.

Table 2. Source parameters of the three events studied.

Event	(strike, dip, rake)	Source time function (s)	Depth (km)	Reference
Utah	(180°, 50°, 250°)	(0.5, 0.5)	11	Zhao & Helmberger (1996)
Eureka	(37°, 51°, 282°)	(1.0, 1.0)	11	Dreger (1996, in preparation)
Skull	(185°, 45°, 240°)	(1.0, 1.0)	11	Zhao & Helmberger (1996)

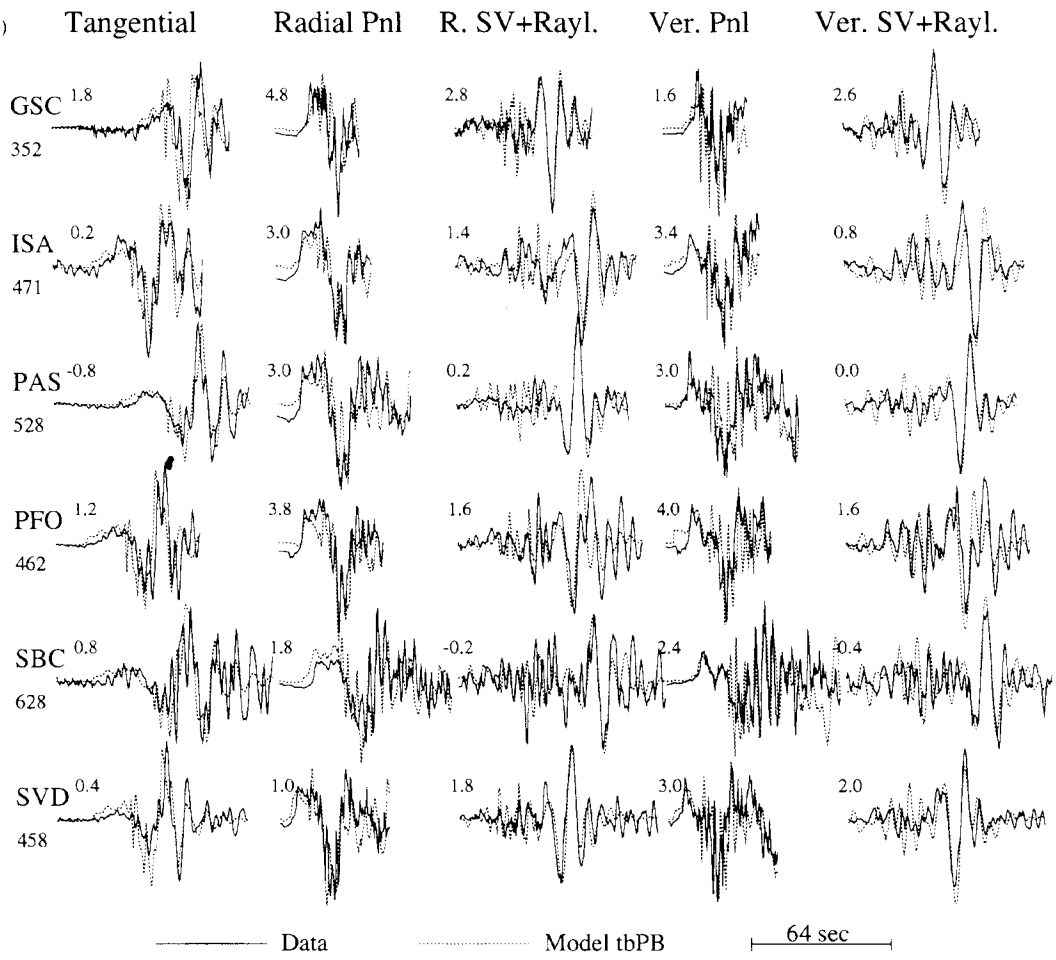

Figure 9. (*Continued.*)

Head waves are produced by the lower interface, along with more high-frequency signals that complicate the P_{nl} portion of the seismograms. Although reflections and multiples from the deep interface overwhelm the up-going P energy, the long-period feature of the P_{nl} wave does not change much. As for surface waves, the slow groups with shorter periods are not very sensitive to the appearance of this deeper discontinuity, but the fast groups with longer periods change significantly. This is because longer-period surface waves sample deeper parts of the crust. The introduction of another deeper discontinuity (Fig. 4b) changes the seismograms in a similar manner; it again adds another head-wave group to the seismograms and complicates them even more.

Systematic perturbation of a crustal model

To build a more direct relationship between model parameters and the seismogram segments, we conduct, in this section, a systematic perturbation of a typical crustal model (model *PB*, Table 1). This model was derived by Priestley & Brune (1978) in their surface-wave studies of the Basin and Range province and was proven effective in more recent waveform studies of this region (e.g. Zhao & Helmberger 1996). Since a small change in velocity of a thick layer produces a large change in traveltime, we attempt to minimize this effect by conserving vertical traveltime differentials. Thus, we perturb the crustal velocities of this model in such a way that, for each layer, the product of the thickness and the percentage change of the velocity is the same, with the exception that changes to the mantle velocities are fixed at 5 per cent. Seismograms computed from the original model and those from the perturbed models are compared in Fig. 5. To quantify the comparison, we cut the radial and the vertical components into three segments: the P_{nl} wave, the SV wave, and the Rayleigh wave. The tangential component is compared as a whole and is referred to as the Love wave for simplicity. In the comparison, each pair of seismogram segments is cross-correlated in order to determine the relative time shift between them. This shift, compared to the starting time of the corresponding segment, is referred to as the time effect of the perturbed velocity on the same segment. After the two segments are shifted correctly relative to each other, an error value, defined as an average of the L_1 and L_2 norm (Zhao & Helmberger 1994) and defining the shape misfit between them, is calculated. This is then referred to as the shape effect of the perturbed velocity on the corresponding segment. Fig. 6 summarizes the quantitative results of these comparisons.

While the results in Fig. 6 are consistent with those qualitative ones that we discussed before, there are a few details that are of interest. As seen in Fig. 6, the P_{nl} wave contains information about most of the crust, but the overall timing of this phase group is mostly controlled by the middle part of the crust. The SV wave, on the other hand, is not sensitive to the crustal P velocity; its timing and shape are controlled

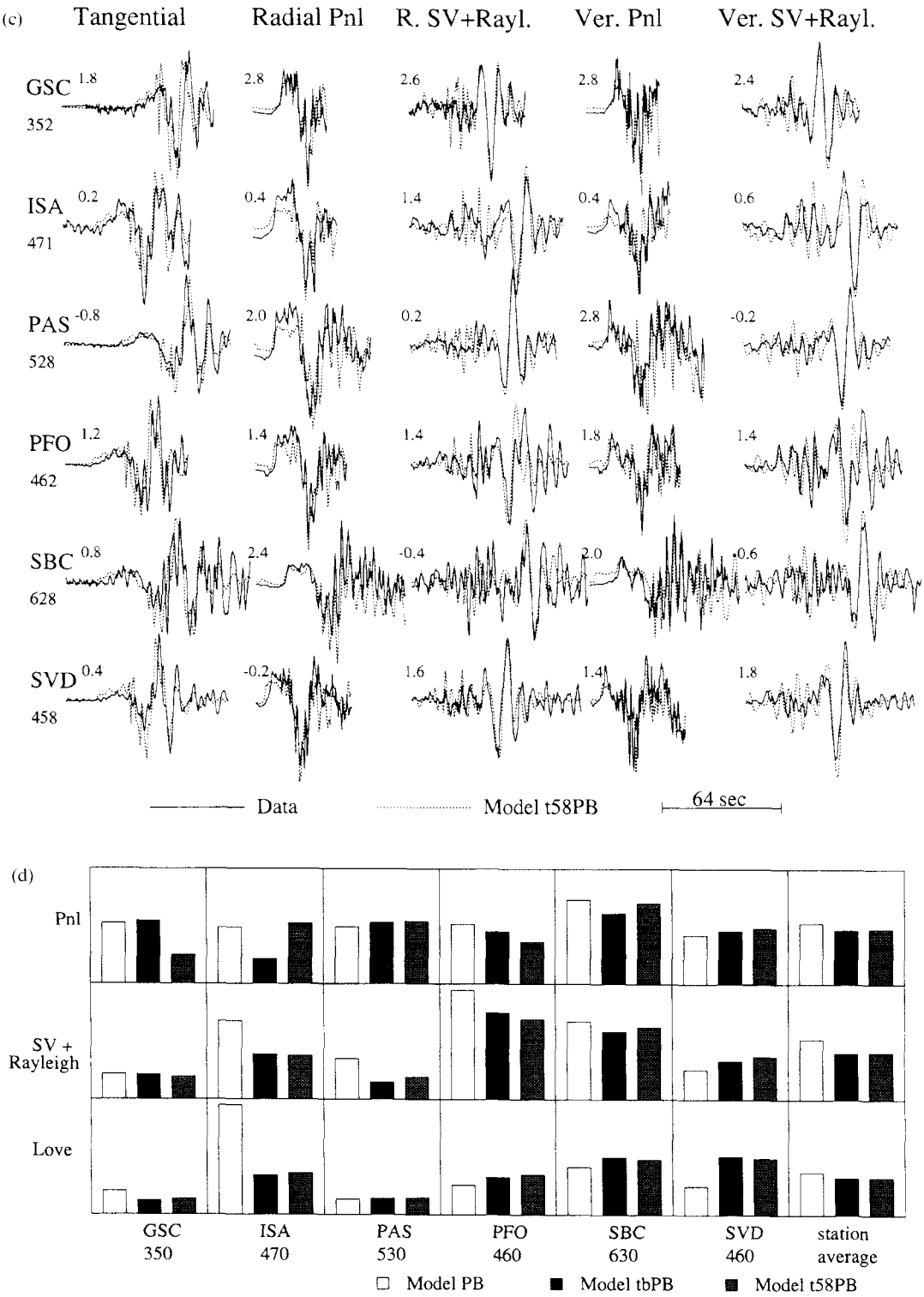

Figure 9. *(Continued.)*

by the shear velocity of the lower crust. While the surface layer has great influence on all segments of a seismogram, it has the greatest impact on the surface waves. In contrast to the *SV* waves, surface waves are less sensitive to the structure below the source depth. Their shape is mostly controlled by the crust above the source depth and their timing is most sensitive to the shear velocities of these layers. Note, though, that it is the *P* velocity of the top layer and the *S* velocity of the layer just above the source depth that control the Rayleigh waves. Perturbation of the mantle velocities (Figs 5i and 5j) reveals that the *P* velocity of the upper mantle only slightly affects the beginning part of the P_{nl} waves but the *S* velocity has a substantial impact on the *SV* segments.

We get similar results with a corresponding set of perturbations of thicknesses, holding the velocities constant. Note that this is a range-dependent effect and does not apply at less

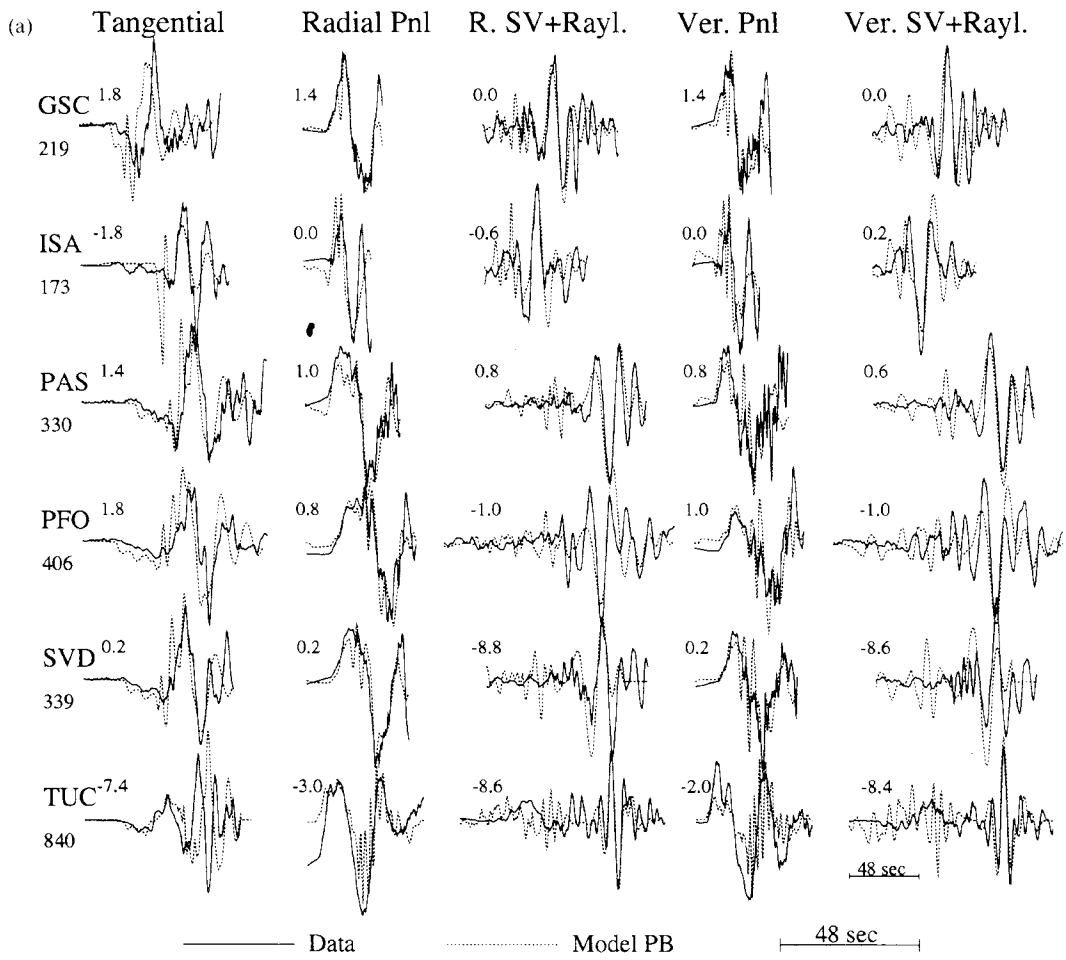

Figure 10. (a) Comparison between displacement data and synthetic waveforms (Model *PB*) for the Eureka Valley event. (b) Comparison between displacement data and synthetic waveforms (Model *tbPB*) for the Eureka Valley event. (c) Shape misfit between data and synthetic waveforms for models *PB* and *tbPB* for the Eureka Valley event.

than 150 km, since the critical angle for the Moho reflection strongly depends on both the crustal velocity and the Moho depth. At distances beyond the critical angle, there is considerable trade-off between the thickness and velocity of each layer. For this reason, we will neglect these sensitivity tests in the interest of brevity.

Sensitivity tests on the Moho transition and the uppermost mantle structure

To examine the effect of the crust–mantle transition on regional seismograms, or the resolution of regional seismograms to this transitional structure, seismograms from two crustal models are generated and compared (Fig. 7). The difference between model *tbPB* (Table 1) and model *mohoPB* in the transitional structure results in slight changes in the high-frequency signals but not in the long-period signals (Fig. 7). At this distance, earthquakes have to have significant magnitude to be well observed, usually with longer source duration and producing longer-period signals at receivers; therefore, this test suggests that the Moho transitional structure cannot be modelled to high resolution with regional seismograms.

The effect of a velocity gradient in the uppermost mantle is displayed in Fig. 8. As shown in Figs 8(b) and 8(c), when there is a negative velocity gradient, rays reflected from the Moho are weakened by rays that are reflected from the deeper discontinuities below the Moho and have the opposite polarity. The net effect is that the initial amplitude of the P_{nl} waves is reduced (Fig. 8a). When the velocity gradient is positive, the effect is the opposite, as displayed in Fig. 8(d).

In the above exercises, we fixed all other earthquake parameters and conducted our sensitivity tests on model parameters. Further studies also suggest that our results are qualitatively correct for a source–receiver distance range of 300 to 600 km, where the critical angle for the Moho reflection is passed and the surface-wave dispersion is not very significant. Although crustal velocities are very important parameters in modelling regional seismograms, we have to keep in mind that other parameters, such as crustal thickness, source depth, and source finiteness, all contribute to the complexity of the regional broad-band waveforms, as addressed in some recent studies, for example Dreger & Helmberger (1991), Saikia & Helmberger (1996) and Song & Helmberger (1996).

1-D MODELLING OF THE BASIN AND RANGE CRUSTAL STRUCTURE

In this section, we model seismograms from three earthquakes with paths sampling the Basin and Range province (Fig. 2) using 1-D models. The data used in this study are broad-band

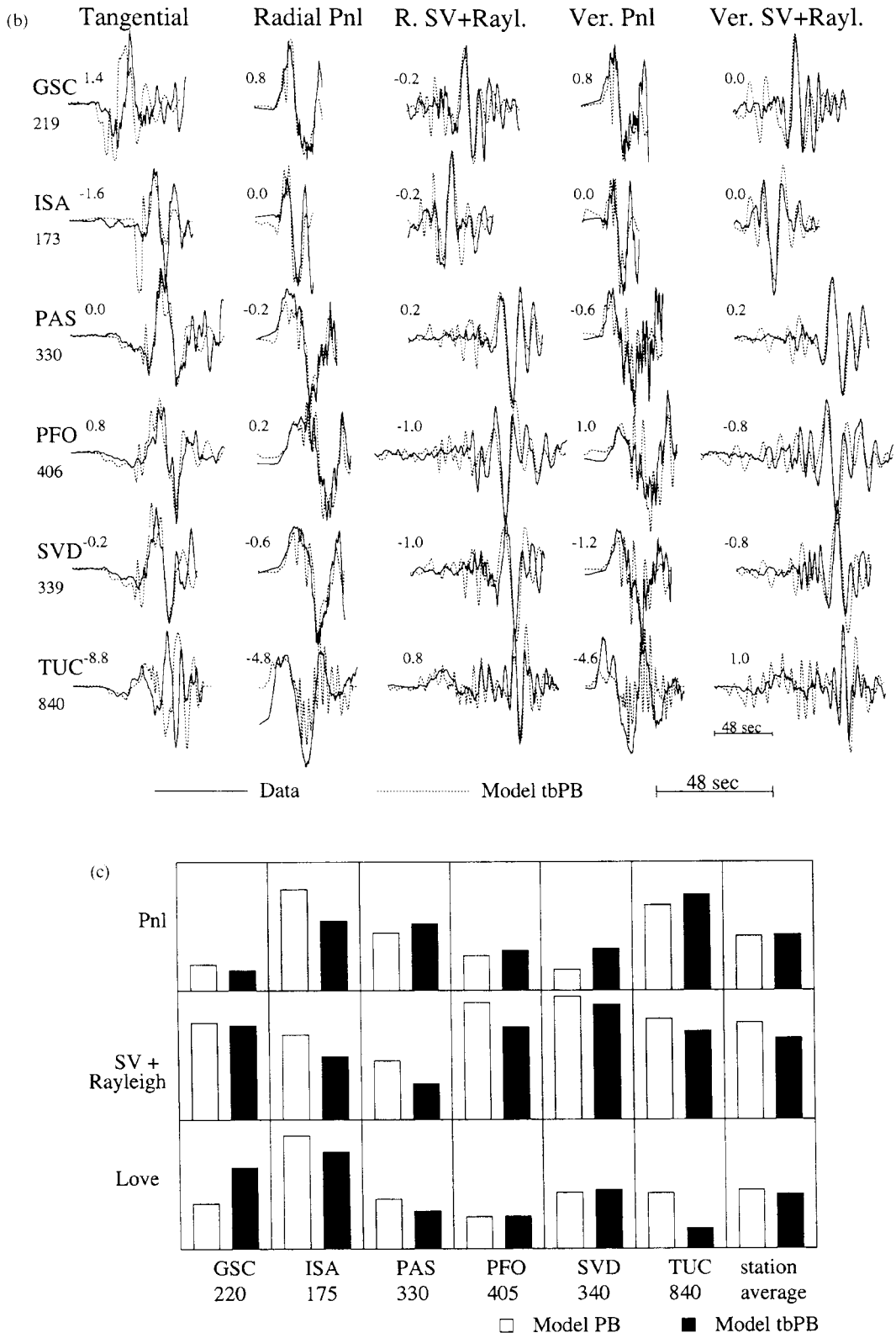

Figure 10. (*Continued.*)

displacement recordings of these earthquakes at seven TERRAscope stations. Event locations and origin times (Fig. 2) are extracted from the TERRAscope network with the source parameters predetermined by other authors (Table 2). In the modelling process, the criteria discussed in the last section are used for the time shift and the shape misfit, except that the *SV* wave and the Rayleigh wave are combined to avoid instability in the cross-correlation procedure. To begin with, we select the Priestley & Brune (1978) model (model *PB*, Table 1), as a reference model. Generally, this is a good average structure in

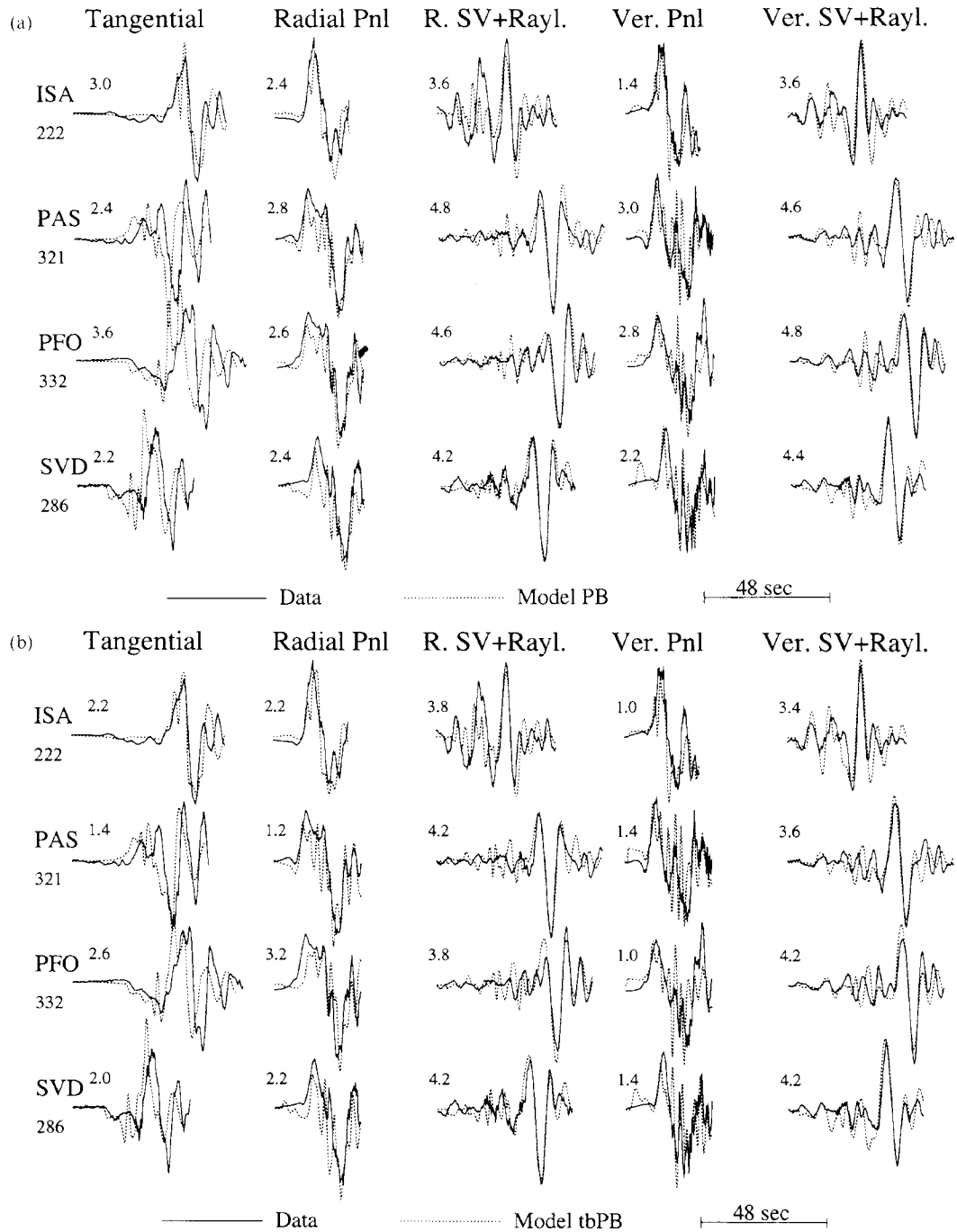

Figure 11. (a) Comparison between displacement data and synthetic waveforms (Model *PB*) for the Skull Mountain event. (b) Comparison between displacement data and synthetic waveforms (Model *tbPB*) for the Skull Mountain event. (c) Shape misfit between data and synthetic waveforms for models *PB* and *tbPB* for the Skull Mountain event.

modelling propagation paths in the Basin and Range province (Zhao & Helmberger 1994). Wave shape, especially that of the surface waves, produced by this model fits the data well when the proper shift is applied (e.g. Fig. 1). However, the timing predicted by this model is not very satisfactory. While this model is too slow for the paths in the southern Basin and Range province, it is too fast for paths in the central Basin and Range province. Also, the relative timing between the P_{nl} waves and the Rayleigh waves in the synthetics are often misaligned by a few seconds when compared to the data (Fig. 1). In our exercise to model the paths in the central Basin and Range province, we seek to decrease the crustal velocity in order to improve the timing prediction, as well as to improve the waveform fits.

We begin by perturbing the top layer of the model. In our grid-search approach, we find that the top layer thickness can range from 2.5 km to 3.5 km with appropriate velocity trade-off. A more significant change to the top layer would result in too much change in the surface-wave shape and timing, especially for the Rayleigh waves. This feature is

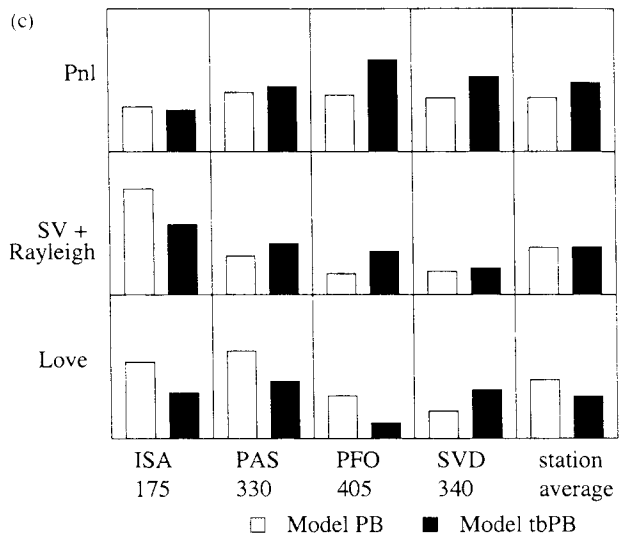

Figure 11. (*Continued.*)

consistent with the conclusion we derived earlier. We also find that the synthetic waveform fits to the data get worse for a larger velocity jump from the upper crust to the lower crust when it is produced by decreasing the upper crustal velocity alone. Next, we decrease the velocities in the lower crust to delay the synthetic waveforms and to adjust the relative timing between the P_{nl} wave and the Rayleigh wave. We find that when the lower crustal velocities are decreased to be the same as those of the upper crust, the resulting simple-crust model is efficient in achieving both goals. Parameters of our preferred model, the *tbPB* model, are given in Table 1 and the time shifts required for the best-fitting synthetics are given for each segment in Figs 9–11.

The Utah event

Zhao & Helmberger (1996) found that the *PB* model did better than the standard Southern California model in modelling this earthquake. In our study, we find that model *PB* is not slow enough, especially for the P_{nl} waves. When the Conrad discontinuity is removed, the timing of the P_{nl} waves and the separation between the P_{nl} wave and the Rayleigh wave are both improved substantially. The average shape misfit to the data is also reduced (Fig. 9d), with the most improvement at station ISA for all three segments. Note that the improvement in the wave shape of the Airy phase at station PFO eliminates the instability factor and reduces the time shift. For model *tbPB*, the timing difference between different segments on the synthetics is reasonably compatible with that in the data, but the synthetics themselves are still too fast. As we further slow down the main crust V_p, as in model *t58PB*, the predicted timing is even better, with the wave shape fits being equally good (Fig. 9d).

The Eureka Valley event

For this event, model *PB* gives good timing predictions but model *tbPB* does even better (Figs 10a and 10b). The slower lower crust in model *tbPB* also improves the waveform fits, especially for station ISA (Fig. 10c). For station SVD, the Rayleigh-wave timing problem of model *PB* is fixed as the relative strength of the two picks on the Rayleigh wave train is adjusted by model *tbPB*. This is also true for the Rayleigh waves at station TUC.

The Skull Mountain event

Among the three events studied, paths from this event to the various stations are the most difficult to model with a 1-D model. Although the *tbPB* model does a little better than the *PB* model, it is still too fast, especially for the Rayleigh waves (Figs 11a–c). The Love waves are better modelled in timing than the Rayleigh waves, but the wave shape is not satisfactory. The positive time shift would suggest a slower model than *tbPB*, but our tests show that further slowing down the main crust, as in model *t58PB*, would make the wave shape even worse, while only slightly improving the timing prediction. This is probably a case where lateral variation has a significant effect. At this stage, we prefer model *tbPB* as an average 1-D model for these paths. Detailed 2-D modelling would be informative.

DISCUSSION

Throughout the modelling in this study, we focused on 1-D models. Simple two-layer models worked well and we do not see any advantage in adding a Conrad discontinuity for paths from the three events to the various stations. Detailed studies by Mori & Helmberger (1996), who analysed direct *S* and *SmS* energy from the 1992 Landers aftershocks recorded at stations GSC and PFO, reported compatible results. They found that *SmS* phases at station GSC are much stronger than the direct *S* phases but that the reverse is true at station PFO. They attribute these observations to the more homogeneous crustal structure in the Mojave desert north of the Landers aftershocks, which allows large reflections from the Moho. From our modelling, we conclude that a Conrad is not a regional feature in the crust of this area.

However, that does not mean the whole crust in the Basin and Range is as simple as our 1-D models. Actually, the time shifts between the different portions of the data and the synthetic waveforms for individual paths in Figs 12(a)–(c) indicate complicated lateral variations in the crustal velocity and crustal thickness. As seen in Fig. 12(a), the P_{nl} timing, which is controlled by the velocity in the mid-crust, reveals that the crust under the Sierra Nevada is faster than that under the northern Mojave desert. This feature is well resolved in the tomographic study of Zhao & Kanamori (1992) as displayed in Fig. 12(d).

The Love-wave timing shown in Fig. 12(b) is similar to that of the P_{nl} portion. This is partially due to the fact that, in our analysis, the timing of the tangential component as a whole, along some paths, is controlled by the down-going long-period *S* energy (Figs 10a and 11a), which is controlled by the lower crust. The Rayleigh-wave timing, however, shows a quite different pattern (Fig. 12c). Rayleigh waves from the Skull Mountain event to the various stations arrive substantially late, unlike the P_{nl} waves or the Love wave. This could have resulted from a slower upper crustal *S* velocity or from a slower *P* velocity in the top layer, as indicated in Fig. 6. However, the first explanation is unlikely, since the Love-wave timing is reasonably good. Notice that the waveforms from the Skull Mountain event are the least well modelled in this study; it is possible that the velocity variation in the top layer

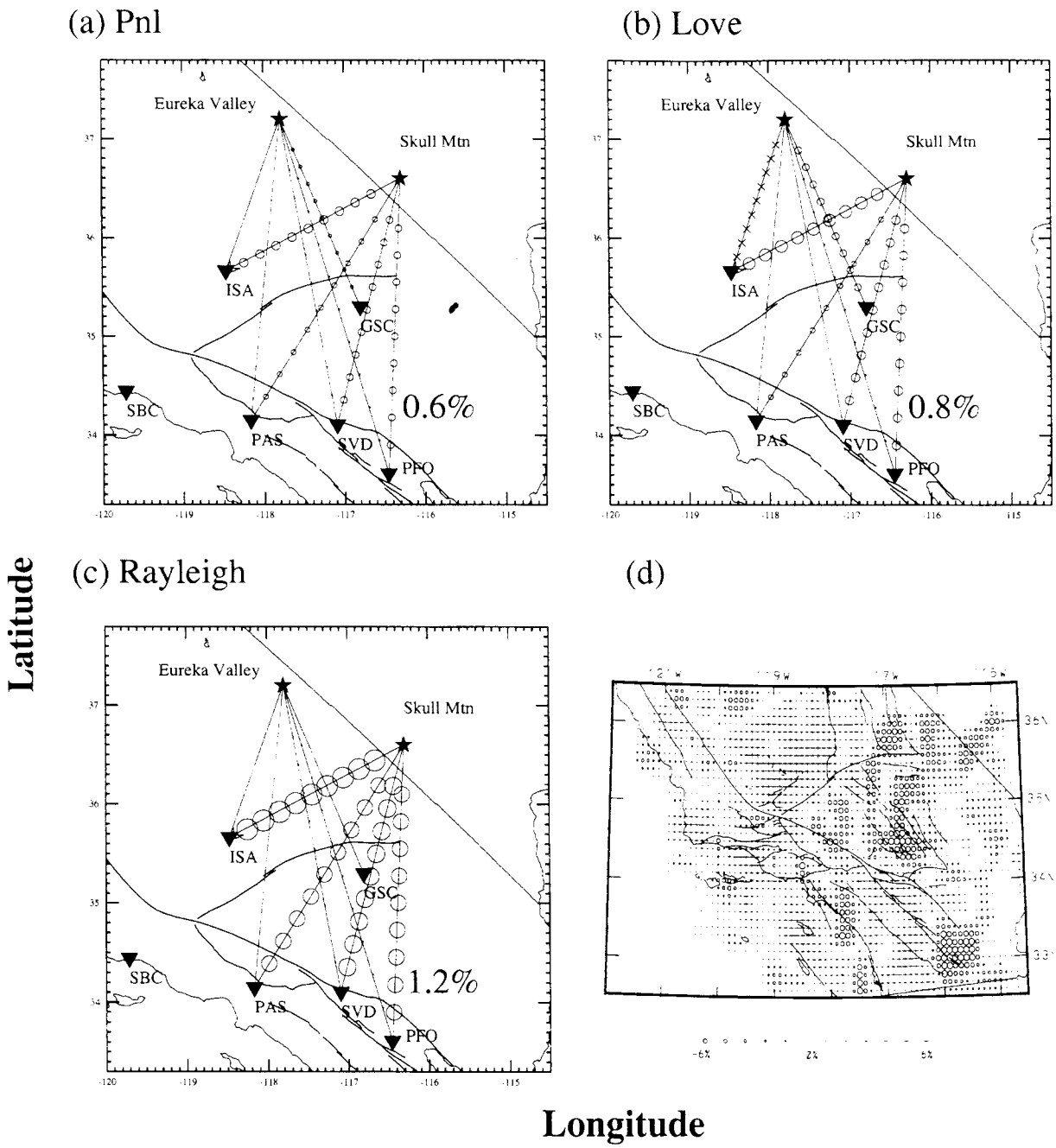

Figure 12. (a)–(c) Integral slowness of individual paths (relative to model *tbPB*), defined as the average time shift (shown in Figs 9b, 10b and 11b) scaled by the source–receiver distance, for each portion of the data. Circles and crosses denote slow and fast paths, respectively. Symbol size corresponds to the integral slowness of the path. For the path from the Skull Mountain event to the station PFO, this value is shown for each portion of the data. (d) A tomographic model for the Southern California crust, showing fractional *P*-wave velocity perturbations (in per cent) at 22 km depth. After Zhao & Kanamori (1992).

along these paths is quite substantial. As we mentioned earlier, data from the Utah event are fit the best by model *t58PB*, while model *tbPB* works the best for paths from the Eureka event. This suggests that the crust under the northeastern Mojave has a smaller Poisson's ratio than the crust under the Sierra Nevada. If this is true, it would partially explain the fact that the Skull Mountain event was the most difficult to model with a 1-D model. The path from the Eureka Valley to the station Tucson (TUC), which runs from near the Sierra Nevada to the northeastern Mojave desert and further to the southern Basin and Range, has this same problem. Detailed modelling for individual paths is necessary to retrieve more detailed information about the crustal structure.

CONCLUSIONS

In conclusion, we have conducted a set of sensitivity tests on the parameters of 1-D models to compare their impact on different segments of regional seismograms. We found that, for mid-crystal earthquakes, P_{nl} waves are controlled in broad-band

character by the mid-crust, while the top layer contributes to the long-period motions. The *SV* wave is mostly controlled by the shear-wave velocity of the lower crust, especially the crustal layer just below the source depth. The top crustal layer controls the shape of the surface waves at ranges from 300 to 600 km, and the upper crust, especially the crustal layer just above the source depth, controls their timing. Applying these tests in the modelling of three earthquakes in the Basin and Range province, we found that a simple two-layer crustal model could effectively explain the data, both in timing and in shape. The main crustal layer has *P* and *S* velocities of 6.1 km s^{-1} and 3.6 km s^{-1}, similar to those found by Langston & Helmberger (1974). A surface layer of thickness 2.5 to 3.5 km is required to fit the Rayleigh waves. Modelling results also indicate that the crust under the northeastern Mojave desert has slower *P* velocity (by 5 per cent) than that under the Sierra Nevada.

ACKNOWLEDGMENTS

We thank Lianshe Zhao for his help throughout this study. Chandan Saikia wrote the modified frequency–wavenumber algorithm. Craig Scrivner, Bradley Woods, Lupei Zhu, David Harkrider, Chandan Saikia, John Cassidy and one anonymous reviewer reviewed the manuscript. This research was supported by the Air Force through grant number F49620-93-1-0221. Contribution No. 5548, Division of Geological and Planetary Sciences, California Institute of Technology, Pasadena, California.

REFERENCES

Dreger, D.S. & Helmberger, D.V., 1991. Complex faulting deduced from broadband modeling of the 28 February, 1990 Upland earthquake (M_L=5.2), *Bull. seism. Soc. Am.*, **81,** 1129–1144.

Dreger, D.S. & Helmberger D.V., 1993. Determination of source parameters at regional distances with three-component sparse network data, *J. geophys. Res.*, **98,** 8107–8125.

Helmberger, D.V., 1983. Theory and application of synthetic seismograms, in *Earthquakes: Observation, Theory and Interpretation*, pp. 173–222, ed. Kanamori, H., Soc. Italiana di Fisica, Bologna, Italy.

Helmberger, D.V., Dreger, D., Stead, R. & Kanamori, H., 1993. Impact of broadband seismology on the understanding of strong motions, *Bull. seism. Soc. Am.*, **83,** 830–850.

Langston, C.A. & Helmberger, D.V., 1974. Interpretation of body and Rayleigh waves from NTS to Tucson, *Bull. seism. Soc. Am.*, **64,** 1919–1929.

Mori, J. & Helmberger, D.V., 1996. Large amplitude Moho reflections (*SmS*) from Landers aftershocks, Southern California, *Bull. Seism. Soc. Am.*, submitted.

Priestley, K. & Brune, J., 1978. Surface waves and the structure of the Great Basin of Nevada and western Utah, *J. geophys. Res.*, **83,** 2265–2272.

Ritsema, J. & Lay, T., 1993. Rapid source mechanism determination of large (M_w>=5) earthquakes in the western United States, *Geophys. Res. Lett.*, **20,** 1611–1614.

Saikia, C.K., 1994. Modified frequency–wavenumber algorithm for regional seismograms using Filon's quadrature-modelling of Lg waves in North America, *Geophys. J. Int.*, **118,** 142–158.

Saikia, C.K. & Helmberger, D.V., 1996. A frequency–wavenumber algorithm to compute up- and down-going wavefields from a buried seismic source, *Bull. seism. Soc. Am.*, submitted.

Song, X.J. & Helmberger, D.V., 1996. Source estimation of finite faults from broadband regional networks, *Bull. seism. Soc. Am.*, in press.

Stead, R., 1990. Finite differences and a coupled analytic technique with applications to explosions and earthquakes, *PhD thesis*, California Institute of Technology, CA.

Zhao, D. & Kanamori, H., 1992. *P*-Wave image of the crust and uppermost mantle in Southern California, *Geophys. Res. Lett.*, **19,** 2329–2332.

Zhao, L.S. & Helmberger, D.V., 1994. Source estimation from broadband regional seismograms, *Bull. seism. Soc. Am.*, **84,** 91–104.

Zhao, L.S. & Helmberger, D.V., 1996. Regional moments, energy levels, and a new discriminant, *Pure appl. Geophys.*, February 1996.